



Article

Computed Tomography of Scheelite Ore, Kara, Australia: Morphological Characterisation and Modal Mineralogy

Leonard T. Krebbers ^{1,*} , Julie A. Hunt ² and Bernd G. Lottermoser ¹ ¹ Institute of Mineral Resources Engineering, RWTH Aachen University, Wüllnerstraße 2, 52062 Aachen, Germany² Centre for Ore Deposit and Earth Sciences (CODES), University of Tasmania, Private Bag 79, Hobart, TAS 7001, Australia; julie.hunt@utas.edu.au

* Correspondence: krebbers@mre.rwth-aachen.de

Abstract: Metal ores are mineralogically characterised to understand their genesis in order to allow informed decisions on mineral processing and to recognise likely environmental risks upon mining. However, standard mineralogical techniques generate only two-dimensional information at best, which in addition may be subject to sampling and stereological errors. By contrast, computed tomography (CT) is a non-destructive imaging technique that allows three-dimensional analysis of solid materials. In the present study, two ore types of the Kara Fe-W deposit (Australia) were characterised using CT to examine their mineral texture and modal mineralogy as well as scheelite distribution and ore grade (WO₃). The results show that scheelite is primarily associated with hydrous phases (e.g., epidote, chlorite, amphibole) and occurs as massive or disseminated mineral as well as vein-fill at minor and trace concentrations. This study demonstrates that CT of scheelite ore enables accurate 3D texture visualisation (volume, grain size distribution) and yields valid quantitative data on modal mineralogy and WO₃ grade of individual ore samples. Consequently, CT analysis of scheelite-bearing ore provides information relevant for ore genesis studies and comminution strategies for the possible recovery of scheelite as a by-product from metalliferous ores.

Keywords: computed tomography; ore geology; 3D imaging; scheelite; critical raw materials



Citation: Krebbers, L.T.; Hunt, J.A.; Lottermoser, B.G. Computed Tomography of Scheelite Ore, Kara, Australia: Morphological Characterisation and Modal Mineralogy. *Minerals* **2024**, *14*, 345. <https://doi.org/10.3390/min14040345>

Academic Editors: Glenn Bark and Alan R. Butcher

Received: 5 March 2024

Revised: 21 March 2024

Accepted: 25 March 2024

Published: 27 March 2024



Copyright: © 2024 by the authors. Licensee MDPI, Basel, Switzerland. This article is an open access article distributed under the terms and conditions of the Creative Commons Attribution (CC BY) license (<https://creativecommons.org/licenses/by/4.0/>).

1. Introduction

Tungsten, a brittle steel-grey metal, is primarily found in nature in wolframite and scheelite, with the latter contributing over 65% to known tungsten deposits [1]. Widely used in various technological applications, such as X-ray tubes, nuclear reactors, and high-performance magnets, tungsten is deemed a critical raw material (CRM) by many advanced economies, exhibiting the highest economic importance according to the EU's CRM evaluation [2]. China is responsible for 85% of the global supply, holding 47% of the world's tungsten resources. Australia ranks second at 11%, with significant deposits found in various regions scattered across the country, such as Queensland, New South Wales, the Northern Territory, and Tasmania [3,4]. Despite this, Australia contributes to only 1% of the global tungsten supply with three operating mines: Kara mine, King Island (both Tasmania), and Mount Carbine (Queensland) [5]. In fact, until late 2023, the Kara mine was the sole production site [5].

To efficiently extract mineral resources, ores must be accurately characterised in order to assess ore deposit quality and to maximising recovery [6]. Methods for analysing tungsten ores encompass a range of conventional techniques including X-ray powder diffraction (XRD), ultraviolet light, electron probe micro-analysis (EPMA), scanning electron microscopy with energy dispersive spectroscopy (SEM-EDS), cathodoluminescence (CL), inductively coupled plasma mass spectrometry (ICP-MS), laser ablation inductively coupled plasma mass spectrometry (LA-ICP-MS), and optical microscopy (OM) (e.g., [7–9]). These methods yield essential insights into the mineralogy, mineral chemistry,

and geochemistry of tungsten ores. However, some techniques, like XRD, may not provide dimensional geometries of the analysed samples. Contrastingly, OM, SEM-EDS, and EPMA offer two-dimensional (2D) visualisation of tungsten ores. Yet, these methods are time-consuming, involve destructive sample preparation, and necessitate careful sectioning of original samples to select representative sample material. Furthermore, translating results from these methods into the third dimension can introduce stereological bias, which can be particularly challenging for low-grade ores with complex mineralogy and microstructure.

X-ray computed tomography (CT) enables the analysis of both bulk and spatially resolved microstructures of scanned objects based on the X-ray attenuation information of its components [10]. It allows for the non-destructive three-dimensional (3D) visualisation and quantitative analysis of microstructural features in situ [10]. Over the past two decades, the technique has been successfully employed in numerous geological investigations [11–15]. CT has also proven its added value to the study of various ore types, particularly those comprising target minerals that exhibit significant attenuation contrast between ore and gangue minerals [16–19]. To date, CT has been applied for measuring the tungsten content of a scheelite ore [20,21] and its concentrate [22].

This study presents the first 3D reconstruction and quantitative analysis of scheelite ores from the Kara Fe-W deposit, Australia, using high-resolution CT. To date, there have been few studies, including technical reports on this deposit, that focussed on mapping, resource and reserve estimation, and formation history [23–27]. This research provides original insights into the volumetric and microstructural features of its tungsten ore minerals. Furthermore, it also introduces the application of a deep-learning-based segmentation workflow for scheelite ore analysis that may be adapted to tungsten ores of similar composition. The ore grades (WO_3) calculated using CT were validated using inductively coupled plasma optical emission spectrometer (ICP-OES) analysis. As a consequence, results of this study extend our existing knowledge of scheelite deposits and contribute to the development of advanced analytical protocols for the characterisation of metals ores.

2. Geological Background

2.1. Regional Geology

The Kara area's regional geology is characterised by Late Precambrian to recent volcano-sedimentary sequences and Devonian granitoids [28]. Precambrian rocks, forming the basement, consist of quartzose lithic wacke, phyllite, and minor dolomite. Cambrian to Lower Devonian units unconformably overlie the Precambrian rock and include the Success Creek Group (siliceous sandstone, mudstone, dolomite, and breccia) and the Criemson Creek Formation (mafic volcanic and volcano-sedimentary rocks) [26]. Overlying Ordovician to Lower Devonian rocks comprise the Mathinna Beds and the Wurawina Supergroup, further divided into the Denison, Gordon, and Tiger Groups [29]. The Denison Group features conglomerate, sandstone, siltstone, and argillite; the Gordon Group consists of carbonates; and the Tiger Group comprises quartzite with limestone fragments. Tertiary basalt and recent sand and gravel cover the area, concealing older units and mineralisation [29]. The Husetop Granite is an important Devonian granitoid located in northwestern Tasmania [26]. It intrudes volcano-sedimentary successions ranging from Precambrian to Lower Devonian. The granite is associated with many carbonate replacement deposits, including scheelite skarns and others. The deposits are located within 1 to 1.5 km from the intrusion [30], suggesting a spatial association with structurally weak zones [31].

2.2. Deposit Geology

The Kara Fe-W deposit is located in northwestern Tasmania, Australia ($41^{\circ}18' S$, $145^{\circ}48' E$) (Figure 1). The Kara deposit area's geology features Cambrian rocks to the northwest, comprising laminated cherty mudstone with carbonates, locally transformed to hornfels or marble and, in places, to metamorphic skarn assemblages [26]. Ordovician units comprise massive and poorly bedded Owen Conglomerate and massive to weakly

bedded and argillaceous Moina Sandstone, as well as impure limestone (Gordon Subgroup equivalent). Devonian granite is exposed in open cuts and often occurs in contact with skarns and showing alteration toward its margin. The granite consists of K-feldspar, quartz, and plagioclase, as well as accessory minerals like biotite, muscovite, epidote, hornblende, and magnetite. Amphibole appears to replace biotite. The granite generally shows an increasing intensity of alteration towards its margin, with feldspars altered to sericite or epidote. Calcite and fluorite are also present as veins in the altered zone. The Kara magnetite–scheelite deposit comprises several NNE-SSW trending skarn bodies (Figure 1A), primarily developed within carbonates, sandstone, impure limestone, or transitional beds in the lower part of the Gordon Limestone. The skarns are in direct contact with the granite but may be separated from it by a thin layer of Owen Conglomerate or Moina Sandstone away from the contact (Figure 1B). The Cambrian and Ordovician sequences were folded during Mid-Palaeozoic deformation, and these fold structures have been intruded by Devonian granite. Post-granite emplacement faulting includes dextral and thrust faults with small displacements [32].

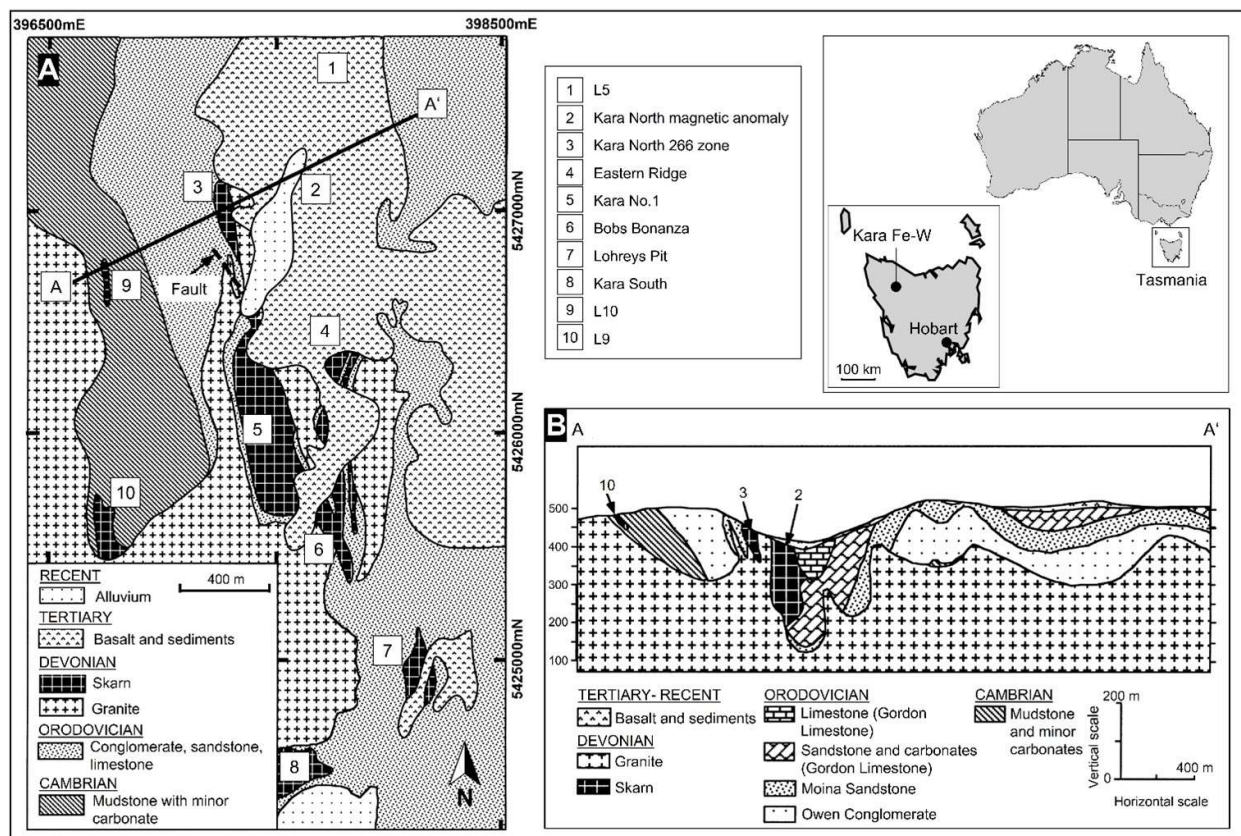


Figure 1. Geological map (A) and geological cross-section (B) of the Kara Fe-W deposit area. Kara No. 1 is the sole orebody being mined. Modified after [26].

Mining at Kara is by open cut and operated by Tasmania Mine Pty Ltd., with magnetite primarily mined and scheelite being extracted as a by-product (of magnetite processing operations). Mining has been focused on the Kara No. 1 orebody since extraction began in 1977. Estimates from a company report from 2016 show the total remaining mineable reserves of 9.9 Mt ore, averaging >30% of Fe, and averaging 378 ppm of WO_3 [24]. In 2018, the tungsten reserves were 3.66 kt WO_3 and a production of 0.025 kt WO_3 [4].

2.3. Deposit Mineralogy

The primary skarn minerals at Kara include magnetite, garnet, vesuvianite, clinopyroxene, epidote, and amphibole, along with subordinate or accessory minerals such as fluorite,

calcite, quartz, scheelite, hematite, chlorite, wollastonite, sphene, pyrite, chalcopyrite, and apatite [26,27]. At least four stages of Skarn formation have been recognised at Kara (Table 1; [27]). Early skarn mineral facies, like garnet and pyroxene, underwent complete or partial replacement by later minerals, such as amphibole, epidote, and chlorite. According to [26], later minerals have developed by pervasive and diffusive replacement of earlier minerals, with a minor contribution from filling vugs, veins, and fissures. Early mineral facies are largely anhydrous, while later ones are predominantly hydrous. A detailed description of macroscopic and microscopic textural features of all mineral assemblages can be found in [24]. In the following, the major and minor occurring minerals of the stage III skarn formation are briefly summarised, as most of the scheelite deposition occurred during that stage [26]. In stage III, scheelite forms very coarse grains locally in excess of 5 cm and shows mutual grain boundaries with other stage III minerals. Magnetite is the most abundant mineral in stage III and shows grain sizes from fine (0.2 mm) to coarse (15 mm); occurs with amphibole; replaces earlier mineral assemblages; and forms as massive aggregates, fractures, or veins. Amphibole is primarily associated with scheelite and magnetite and occurs in hand specimens as fine to coarse grained (up to 5 mm) aggregates. Anhydrous epidote shows mutual existence with other stage III minerals and exhibits variable grain sizes (0.2–10 mm). Fluorite is primarily associated with amphibole, epidote, and chlorite. Its grain size ranges from 0.1 to 5 mm.

Table 1. Mineral assemblages of the identified skarn formation stages after [27]. Note that minor chalcopyrite and bornite may also occur in the mineral paragenesis of skarn formation stage III.

Skarn Formation Stage	Paragenesis
Stage I	Clinopyroxene ± garnet ± vesuvianite ± wollastonite ± quartz ± scheelite
Stage II	Garnet-vesuvianite-magnetite ± scheelite ± apatite ± quartz
Stage III	Magnetite-amphibole-epidote-fluorite-quartz ± chlorite ± garnet ± vesuvianite ± scheelite ± carbonate ± pyrite ± clinopyroxene
Stage IV	Hematite ± fluorite ± calcite ± quartz

3. Materials and Methods

3.1. Conventional Analysis

Two ore samples from the Kara mine were collected on site from the run-of-mine (ROM) stockpile, reflecting two types of mineralisations: (1) a scheelite-bearing feldspar-rich host rock, and (2) scheelite-bearing magnetite ore. UV light was utilised during sample collection to confirm the presence of scheelite. Two polished mounts were prepared for automated mineralogy using the FEI MLA 650 scanning electron microscope (FEI Company, Hillsboro, OR, USA) equipped with two Bruker XFlash 5030 detectors operating at 20 kV and 7 nA. For quantitative mineralogical analysis, the Advanced Mineral Identification and Characterization System (AMICS) software (v3.1) package was used (Central Science Laboratory, University of Tasmania, Hobart, Australia). As the original sample mounts of the collected ROM material showed none to very minor scheelite on the polished surface (Figure A1), a third polished mount (ROM1) of the collected scheelite-bearing feldspar-rich host rock sample material was prepared as well as the selection of another sample of the collected magnetite ore material (ROM4) for CT analysis (Figure 2). The ROM1 sample was subject to further petrographic analysis using a LEICA DM 2700P polarisation microscope (Institute of Mineral Resources Engineering, RWTH Aachen University, Aachen, Germany) as well as a FEI 650F scanning electron microscope equipped with two Bruker XFlash 5030 detectors operating at 15 kV and 25 kV and 10 nA (Institute of Mineralogy and Economic Geology, RWTH Aachen University, Germany). The final ROM4 sample was directly processed to CT analysis without additional preparation and petrographic analysis. After the initial CT analysis, the samples were subject to XRD and ICP-OES analysis. For XRD analysis, 1.3 g of each sample was ground for 1 min using the TS 250 vibratory disk mill (Siebtechnik GmbH, Mülheim a.d.R., Germany). The micronised specimens underwent quantitative phase identification using the High-

Score Plus software (v. 5.2, Malvern Panalytical, Almelo, The Netherlands) on a Malvern Panalytical Aeris benchtop powder X-ray diffractometer equipped with a Co source that operated at 40 kV and 8 mA (QXRD, Institute of Mineral Resources Engineering, RWTH Aachen University, Germany). XRD patterns were collected from 5 to 80° 2 θ with an acquisition time of 60 min. Mineral phases were identified by referencing the ICDD PDF4 + database. For ICP-OES analysis, the same homogenised samples were subjected to microwave digestion using the MLS TurboWave (MLS Mikrowellen-Labor-Systeme GmbH, Leutkirch, Germany). The acid mixture consisted of 8 mL of inverted aqua regia (3 parts HNO₃, 1 part HCl) and 2 mL of HBF₄ (a hydrofluoric acid substituent). The W standards used had concentrations of 1 g/L and 10 g/L, which were subsequently diluted according to the sample requirements. The calibrated range was 0.1–10 mg/L. The W content of both samples was then measured using the SEPCTRO ARCOS ICP-OES (SEPCTRO Analytical Instruments GmbH, Kleve, Germany; Institute IME Process Metallurgy and Metal Recycling, RWTH Aachen University, Germany).

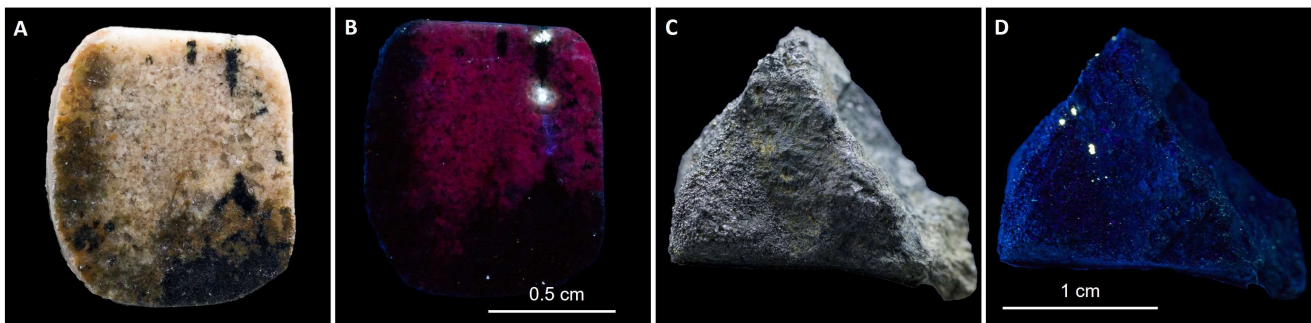


Figure 2. Samples used for CT analysis. (A,B) Polished section of the ROM1 sample (scheelite-bearing feldspar rich host rock); (B) under UV light. The purple and blue fluorescence colours can be attributed to K-feldspar and fluorite, respectively. (C,D) ROM4 sample (magnetite ore); (D) under UV light. In both samples, scheelite is white under UV light, indicating a low concentration of Mo, as reported in [26].

3.2. Computed Tomography

A CT-ALPHA micro-CT system (ProCon X-ray GmbH, Sarstedt, Germany) was utilised, comprising a five-axes-manipulation system between an XWT-240-TCHE plus X-ray tube with a maximum voltage of 240 kV and an XRD 1611 AP3 detector system with 4096 × 4096 pixels (100 mm²) (Institute of Mineral Resources Engineering, RWTH Aachen University, Germany). A specimen is placed between the X-ray source and the detector on the rotating table. During the measurement, 2D sample projections (radiographs) are collected as the specimen rotates 360° around the vertical axis. The detector collects the intensity of transmitted X-ray photons of each projection, providing X-ray attenuation information. From this information, an X-ray attenuation coefficient is calculated for each pixel of the sample projection. This coefficient is displayed as a distinct grey-scale value in the projection image [13]. The acquired radiographs are then processed using a reconstruction algorithm to produce a 3D volume represented by a cubic matrix of grayscale voxels (3D pixels).

The successful application of CT relies on the X-ray beam's ability to penetrate the sample. X-ray attenuation is primarily governed by photoelectric absorption and Compton scattering, and it is influenced by material density, average atomic number, and applied X-ray energy [33]. The photoelectric effect prevails in low energies (approximately 50–100 keV), whereas Compton scattering dominates in energies > 5 MeV [34]. The likelihood of photoelectric absorption is highly dependent on the atomic number (Z), with absorption being proportional to Z^{4–5} [34]. In Compton scattering, the probability of X-ray absorption is proportional to Z, as the incoming X-ray photon interacts with a free or outer electron, ejecting it. Thus, the likelihood of this effect is more reliant on the electron density

of the material [34]. Therefore, higher X-ray energies increase the penetration capacity of the X-ray and reduce beam hardening but may reduce image contrast of less dense and lower Z phases. Given that scheelite, the target mineral, possesses both high average Z and high density, high X-ray energies were applied to both samples (Table 2) to reduce beam hardening caused by the mineral.

Table 2. The two CT scanning parameters used in this study. The acquisition of CT data of ROM1 involved the fusion of two test measurements acquired at 150 kV due to acquisition issues.

Parameter	ROM1		ROM4
Voltage (kV)	150	150	180
Power (W)	8	8	8
Binning (# × #)	2 × 2	2 × 2	2 × 2
Exposure time (s)	1.6	0.8	1.9
Number of projections (#)	1600	1600	1600
Resolution (μm × μm × μm)	7.8	7.8	8.4
Prefilter (-)	Cu0.4 ¹	None	Cu0.4 ¹
Averaging (#)	4	4	12

¹ Cu0.4 = copper filter of 0.4 mm thickness.

Due to acquisition issues for ROM1, an image fusion approach of two test measurements was applied. Image fusion can be used to acquire dual-energy CT (DECT) data by the means of combining attenuation information from single-energy CT scans performed at different energy levels to enhance image contrast [35]. The datasets available in the present study were acquired at the same X-ray energy. However, the linear combination of SECT datasets also involves mathematically merging the pixel values of corresponding projection pictures from each dataset, resulting in higher information density. This reduces the significance of outliers, which in turn reduces the standard deviation and noise in the fused dataset. The scans were fused before reconstruction using

$$f_{FI, \alpha} = \alpha \cdot f_{VA} + ((1 - \alpha) \cdot f_{VB}) \quad (1)$$

where $f_{FI, \alpha}$ represents the fused projection image obtained through a weighted linear combination of the respective scan A (f_{VA}) and scan B projection (f_{VB}). The weighting factor, α , was set to 0.5 to maximise the information density. All raw data collected were reconstructed using Volume Graphics VGStudio Max 3.5.1 [36] applying a beam hardening correction.

Image Processing

To enhance image quality, digital image filters were applied prior to segmentation using ORS Dragonfly (Version 2022.1, [37]). For ROM1, a median filter with a kernel size of 3 was applied to denoise the image. For ROM4, a three-filter combination was used. First, a median filter was applied, followed by the unsharp filter, using an unsharp factor of 3 to increase the edge contrast of grains. Since the unsharp filter produces noise, the median filter was applied again to denoise the image.

Segmentation was carried out using ORS Dragonfly. The software possesses deep learning algorithms that can be used for segmenting different phases simultaneously. Deep learning (DL), a subset of ML, employs interconnected processors (neurons) predominantly built on a convolutional neural network (CNN) architecture, known for its efficiency in image processing [38]. For accurate segmentation results, the network must be sufficiently trained to identify structures and learn how to make predictions (inference stage). Multiple regions of interest (ROI) on various 2D image slices were manually selected to create ground truth data for training and validating the algorithm through supervised classification. Consequently, the network allows for automatic segmentation of the entire dataset. To accelerate the operating time of the segmentation procedure, the size of the volumes was reduced by excluding as much air as possible. For both datasets, a sensor3D model

architecture [39] was chosen and trained. The accuracy of a model and thus the segmentation result depends on the network parameters, which need to be selected properly in accordance with the properties of the data information to be segmented. For each dataset, five classes were determined based on visual differentiating ability and paragenesis. Linear attenuation coefficients (μ) of the phases identified, using AMICS, OM, and SEM-EDS, were calculated (Table 3) to assist the manual labelling process. Initially, each class was labelled using an Otsu-threshold on a representative selected area (frame) of a 2D slice, followed by manual refinement. The model was then tested on a new slice, and any wrongly classified voxels were corrected and attributed to the training data until no further improvement was achieved.

Table 3. Linear attenuation coefficients (μ) as a function of X-ray energy of all minerals identified by AMICS, XRD, UV light, OM, and SEM-EDS. The coefficients were calculated using the XCOM Photon Cross-Sections Database NIST [40].

Mineral	150 kV	180 kV
K-feldspar	0.36	0.34
Albite	0.36	0.34
Kaolinite	0.37	0.35
Quartz	0.37	0.35
Muscovite	0.40	0.37
Fluorite	0.47	0.43
Apatite	0.48	0.44
Actinolite	0.48	0.43
Ferro-edenite	0.48	0.43
Biotite	0.48	0.44
Diopside	0.49	0.45
Epidote	0.51	0.46
Chamosite	0.51	0.45
Ferro-kaersutite	0.52	0.46
Titanite	0.52	0.48
Andradite	0.61	0.54
Chalcopyrite	0.79	0.66
Ilmenite	0.80	0.69
Pyrite	0.86	0.74
Magnetite	0.93	0.79
Bornite	1.02	0.83
Zircon	1.54	1.09
Monazite	2.96	2.00
Scheelite	6.48	4.23

4. Results

Results for scheelite-bearing feldspar-rich (ROM1) and magnetite-rich (ROM4) ores are presented below. First, a petrographic description using CT is given; note that the grey value assignment to the corresponding phases was guided by AMICS data (Figure A1), μ (Table 3), as well as OM and SEM-EDS (ROM1, Figure A2). Second, the modal mineralogy and quantitative microstructural information of scheelite (volume, grain size distribution) are presented. Finally, the tungsten content from each sample is compared with ICP-OES analysis.

4.1. Petrographic Description and Modal Mineralogy

The ROM1 sample comprises a quartz and K-feldspar dominated matrix, together with epidote, chlorite, minor fluorite, and biotite, as well as accessories of titanite, scheelite, ilmenite, zircon, and monazite. The applied acquisition parameters allowed for the visual differentiation between five minerals or mineral groups: (1) quartz; (2) K-feldspar; (3) combined chlorite, epidote, fluorite, biotite, and titanite; (4) combined zircon, monazite, and ilmenite; and (5) scheelite (Figure 3A). In the process of segmentation, a background class (necessary for extracting the volume of the sample) and four mineral or

mineral group classes were defined based on attenuation properties and genetic association, including class (1) = combined quartz and K-feldspar (hereafter referred to as kfs-qz); class (2) = combined epidote, chlorite, fluorite, biotite and titanite (hereafter referred to as ep-chl); class (3) = scheelite; and class (4) = combined zircon, monazite, and ilmenite (hereafter referred to as zr-mnz-ilm). Although the latter exhibits sufficient attenuation contrast (Table 3) to reflect a range of grey values, it was not always possible to clearly distinguish between these phases due to the fact the grey value intensity was influenced by the size of the grains, thus resulting in overlapping grey values.

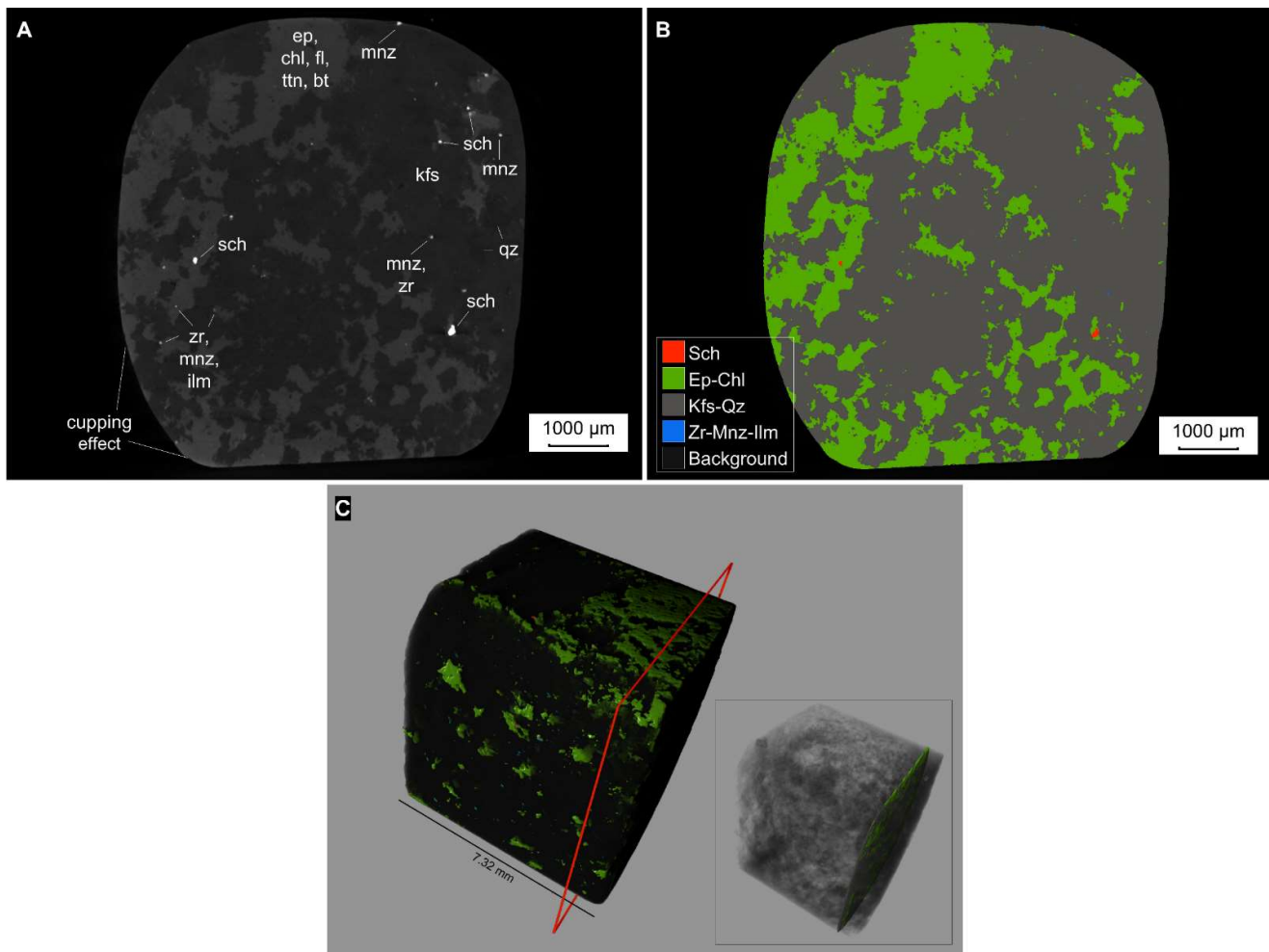


Figure 3. CT volume slice of ROM1 before (A) and after segmentation (B). Volume of ROM1 sample with the position of the CT volume slice, as indicated by the red square and the insert image (C). The thickness of the volume slice in the insert image is 10 µm. Abbreviations: bt = biotite, chl = chlorite, ep = epidote, fl = fluorite, ilm = ilmenite, kfs = K-feldspar, mnz = monazite, qz = quartz, sch = scheelite, ttn = titanite, zr = zircon.

Class (1) shows varying grain sizes (100 µm–2 mm) and exhibits minerals with anhedral to subhedral shapes. In some areas, K-feldspar is overprinted by chlorite (Figure A1). SEM-EDS data indicated that class (2) predominately consists of epidote and chlorite with minor fluorite and trace amounts of titanite. Although chlorite was not identified using XRD, potentially due to its detection limit and the fact that XRD struggles to identify sheet silicates, SEM-EDS data suggest that subhedral epidote (≤ 400 µm) and mostly anhedral chlorite (≤ 700 µm) occur in similar proportions with epidote, partially overprinting chlorite (Figure A2). In the CT data, a pervasive texture was observed with fuzzy grain boundaries (Figure 3A–C). CT further showed that class (2) is spatially heterogeneously

distributed (Figure 4A) as well as in a up to 2 mm thick vein. Euhedral shaped zircon ($\leq 50 \mu\text{m}$) and anhedral monazite ($\leq 40 \mu\text{m}$) occur randomly in the ore matrix (Figure 4B), showing mutual grain boundaries with the other minerals (Figure 3A,B). Anhedral ilmenite is pseudomorphly replacing titanite.

Scheelite occurs disseminated in the silicate matrix (Figure 4C), with grain size ranging from 10.48 to 360.88 equivalent sphere diameter (Equation (2), Table 4). Notably, most of the grains are spatially associated with ep-chl, with the majority of the volume embedded in the vein comprising ep-chl (Figure 4A,D). Apart from its association with chlorite and epidote, some scheelite grains show mutual grain boundaries with quartz and K-feldspar. The scheelite grains are orientated with their length axis parallel with the vein indicating a structurally controlled mineralisation (Figure 4E). Larger scheelite grains show a subhedral to euhedral shape. The shape and the orientation of the smaller particles are not clearly identifiable due to the scanning resolution.

Table 4. Textural properties of scheelite (P (n) = particle number, P (%) = percentage of particles, ESD = equivalent sphere diameter, vol. = volume). The particle volume was manually scaled using the volume classes defined.

Vol. (mm ³)	ROM1					ROM4				
	ESD (μm)	P (n)	P (%)	Vol. (mm ³)	Vol. (%)	ESD (μm)	P (n)	P (%)	Vol. (mm ³)	Vol. (%)
≥ 0.00001	10.13–26.56	36	8.28	0.0002	0.12	10.48–26.42	238	26.65	0.001	0.04
< 0.00001 –0.0001	27.51–57.64	251	57.7	0.01	7.25	26.96–57.5	388	43.45	0.01	0.59
< 0.0001 –0.001	57.75–122.41	134	30.8	0.04	26.16	57.62–126.38	212	23.74	0.06	2.64
< 0.001 –0.01	129.66–265.96	10	2.3	0.03	20.64	126.31–265.69	46	5.15	0.15	6.68
< 0.01 –0.1	282.74–360.88	4	0.92	0.07	45.82	278.67–473.35	5	0.56	0.14	6.08
< 0.1 –1		-	-	-	-	698.62–1238.93	4	0.45	1.94	83.96
Total		435	100	0.15	100		893	100	2.31	100

For the quantitative analysis of the CT data, the volume and voxel count were calculated from the segmented classes. To determine the particle size distribution of scheelite, the equivalent sphere diameter (ESD) was calculated.

$$\text{ESD} = \sqrt[3]{\frac{6 \times \text{volume}}{\pi}} \quad (2)$$

The segmented volume of the ROM1 sample is 458.38 mm³, with silicates making up the largest amount (411.77 mm³) of the whole volume followed by ep-chl (46.34 mm³). Scheelite and zr-mnz-ilm occur as accessories with 0.15 mm³ and 0.12 mm³, respectively. The volumetric proportion of the classes defined of ROM1 is summarised in Figure 5A. Scheelite ranges in grain size from 10.48 to 360.88 μm ESD (Figure 5B, Table 4) with an average size of 57.51 μm and a median of 48.71 μm ESD. The smallest particle has a volume smaller than 0.00001 mm³. The majority of particles (57.7%) exhibits a volume ranging from < 0.00001 to 0.0001 mm³ (Table 4). However, the largest four particles constitute 46% of the total scheelite volume (Table 4), with the largest particle exhibiting a volume of 0.025 mm³.

The ROM4 sample comprises magnetite together with silicates and minor scheelite. According to AMICS and QXRD data (Figures A1 and A3), the silicates mainly comprise amphibole with minor chlorite, andradite, quartz, and epidote, while some quantities of pyrite, chalcopyrite and bornite are also present.

In the CT data, five visually distinguishable minerals or mineral groups were identified: magnetite, scheelite, pyrite/chalcopyrite, bornite, and silicates (Figure 6A). The latter was unable to be further distinguished due to the X-ray setting applied. In the process of segmentation, five classes were able to be defined: background, scheelite, magnetite, silicates, and Fe-sulfides (pyrite, chalcopyrite, and bornite) (Figure 6B). The Fe-sulfides were grouped as a single class due to challenges in clear discrimination by the naked eye, particularly with grains exhibiting replacement textures and smaller sizes (pyrite and chalcopyrite).

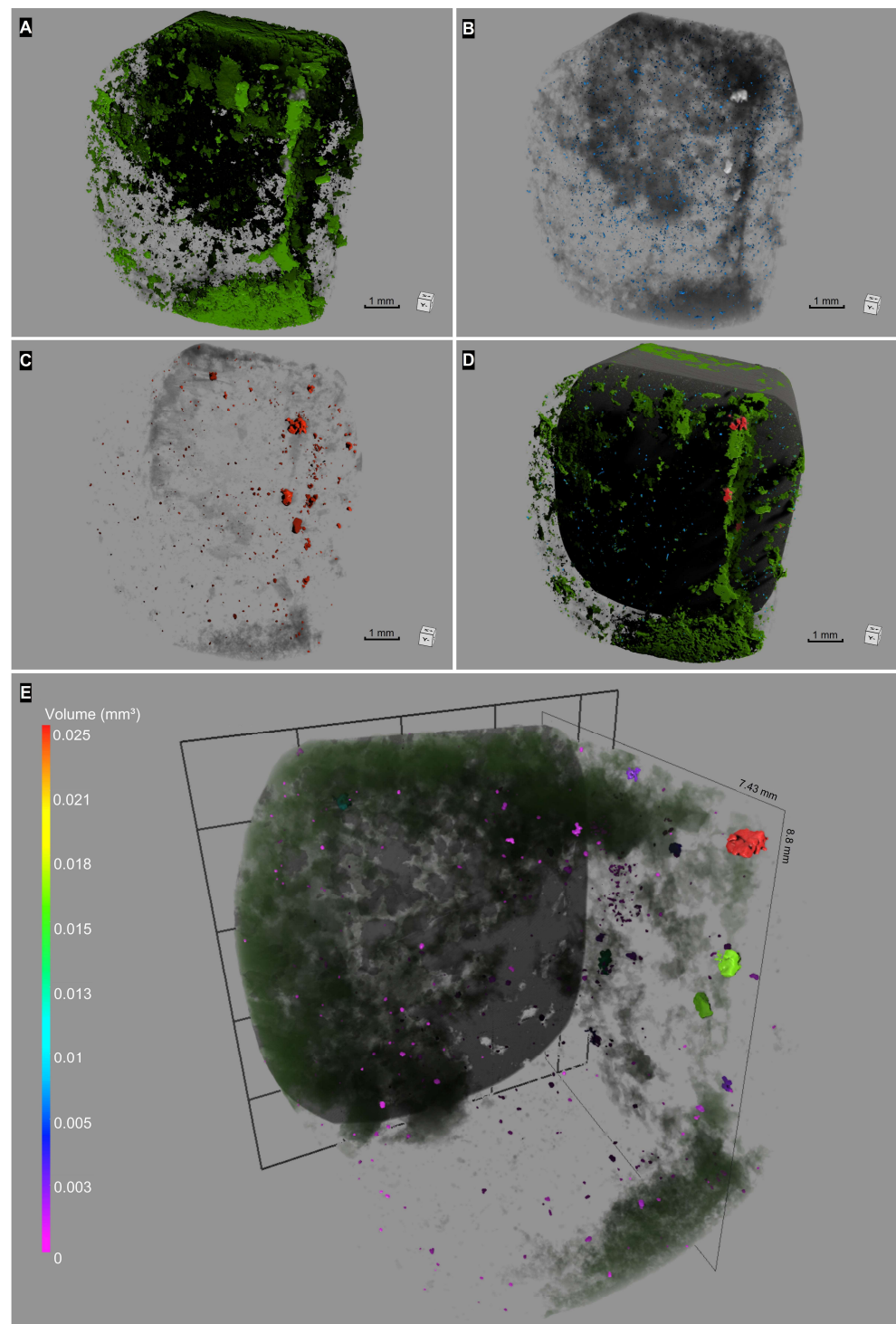


Figure 4. Spatial occurrence of the classes defined for ROM1: (A) Epidote and chlorite with minor fluorite and titanite mainly exhibiting a fuzzy texture. (B) Distribution of accessories comprising combined zircon monazite and ilmenite occurring randomly in the matrix. (C) Disseminated scheelite particles. (D) All classes combined including grey-coloured class consisting of quartz and K-feldspar with minor biotite that is partially clipped. Note that the majority of the scheelite particles are spatially associated with a vein comprising epidote, chlorite with minor fluorite and titanite. All other classes are set semi-transparent (A–C). (E) Volumetric distribution of scheelite particles. Note the spatial association with the ep-chl class (coloured green and set semi-transparent), with most of the scheelite being embedded in a vein, as indicated by the black square.

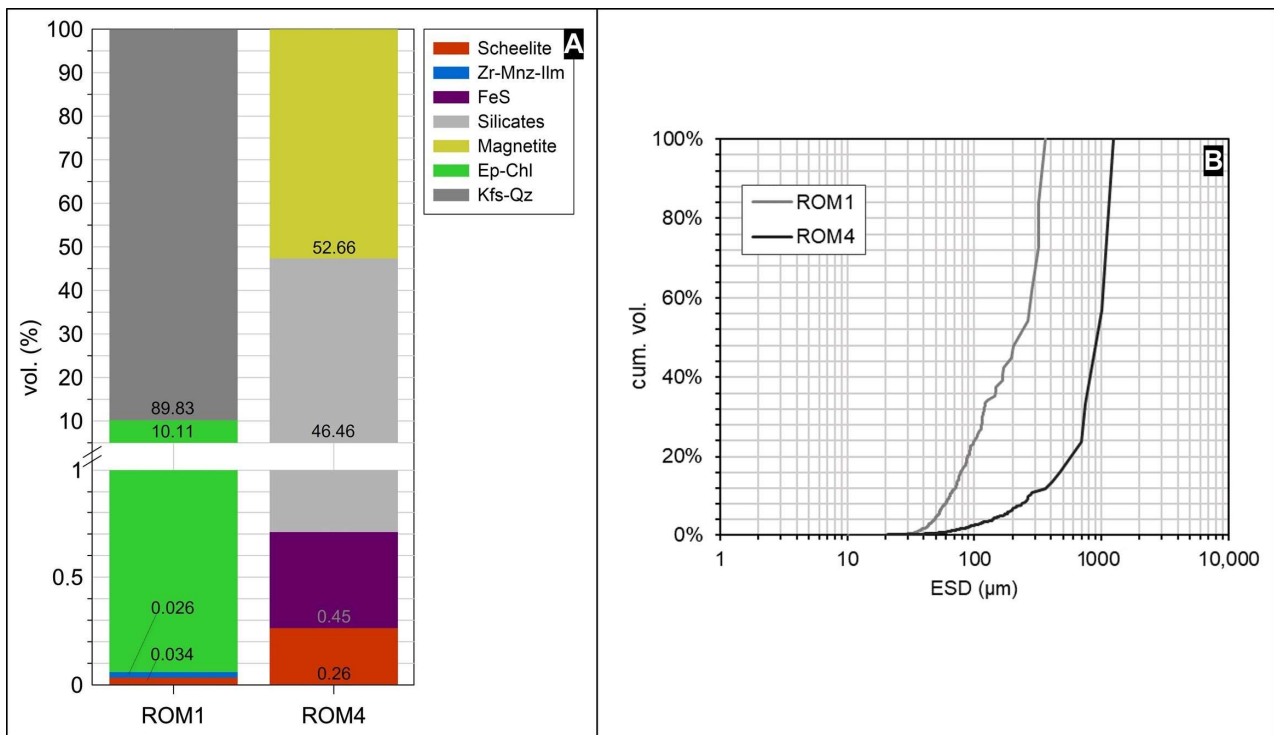


Figure 5. Modal mineralogy (A) and scheelite particle size distribution (B) of the samples investigated as determined by CT. Abbreviations: chl = chlorite, ep = epidote, ilm = ilmenite, kfs = K-feldspar, mnz = monazite, qz = quartz, zr = zircon.

Magnetite exhibits two texture types. It occurs as massive agglomerates with euhedral grains (50 μm –2 mm in length) showing triple-junction grain boundaries and as subhedral elongated, and partially aligned crystals embedded in a silicate matrix (up to 5 mm in length) (Figure 6C). Between the agglomerates of magnetite, silicates are present with minor Fe-sulfides that are separated by a NW-SE trending vein (relative to the top surface of the sample) comprising silicates, Fe-sulfides, and scheelite (Figure 7A–D).

In the vein, scheelite exhibits euhedral to subhedral grains that are elongated parallel to the vein (Figure 7D,E). Within the vein structure, scheelite particles are often attached to each other thereby forming massive aggregates. The segmented 3D image of scheelite revealed that the majority of the scheelite volume is made of a few agglomerates of scheelite grains attached to each other (Figure 7E). A few medium to smaller grains, which are present in different areas than the vein, occur disseminated and predominately associated with silicates that is most likely actinolite and kaersutite according to XRD and AMICS data (Figures A1 and A3). Some particles also share grain boundaries with Fe-sulfides and magnetite. However, it is important to note that most of these particles is in the vicinity of the scheelite vein (Figure 7A).

Pyrite/chalcopyrite was able to be recognised by their texture (Figures 6A and 7B) and their lower X-attenuation compared to magnetite (Table 3). They occur as small anhedral fissures, occasionally displaying replacement textures with silicates. Bornite was able to be distinguished by its higher X-ray attenuation compared to magnetite as well as pyrite and chalcopyrite (Table 3). It is present as small anhedral grains ($\leq 150 \mu\text{m}$) in the silicate matrix that are occasionally attached to magnetite.

The ROM4 sample volume is 879.1 mm^3 . The sample volume is primarily composed of magnetite (462.92 mm^3) and silicates (409.93 mm^3) (Figure 5A). The volume of Fe-sulfides is 3.92 mm^3 and the volume of scheelite is 2.31 mm^3 . Scheelite ranges in grain size from 10.13–1238.38 μm ESD (Figure 5B, Table 4) with an average size of 55.77 μm and a median of 38.36 μm ESD. The sample contains 893 particles. Notably, 84% of the scheelite volume is made of four particles of which two of them contribute to 66.31% of the total scheelite

volume. These are agglomerates attached to each other and or intergrown particles of scheelite grains attached to each other that form the majority of the scheelite vein-fill (Figure 7E).

4.2. Validation

The ICP analyses resulted in WO_3 contents of 0.059 wt% (ROM1) and 0.32 wt% (ROM4) (Table 5). The magnetite content is 60.3% according to CT analysis. This is a difference of 4.3% compared to QXRD (Figure A3). Since the other classes comprise multiple minerals, a comparison was not possible.

Table 5. Tungsten content of the samples investigated as determined using CT and ICP-OES (Sch = scheelite).

Sample	Weight (g)	CT			ICP-OES		Difference in WO_3 Grade (%)
		Sch Vol (mm^3)	Sch wt (g)	WO_3 Grade (wt%)	WO_3 Grade (wt%)		
ROM1	1.3664	0.154	0.000939	0.055	0.059	6.85%	
ROM4	3.961	2.311	0.0141	0.29	0.32	9.12%	

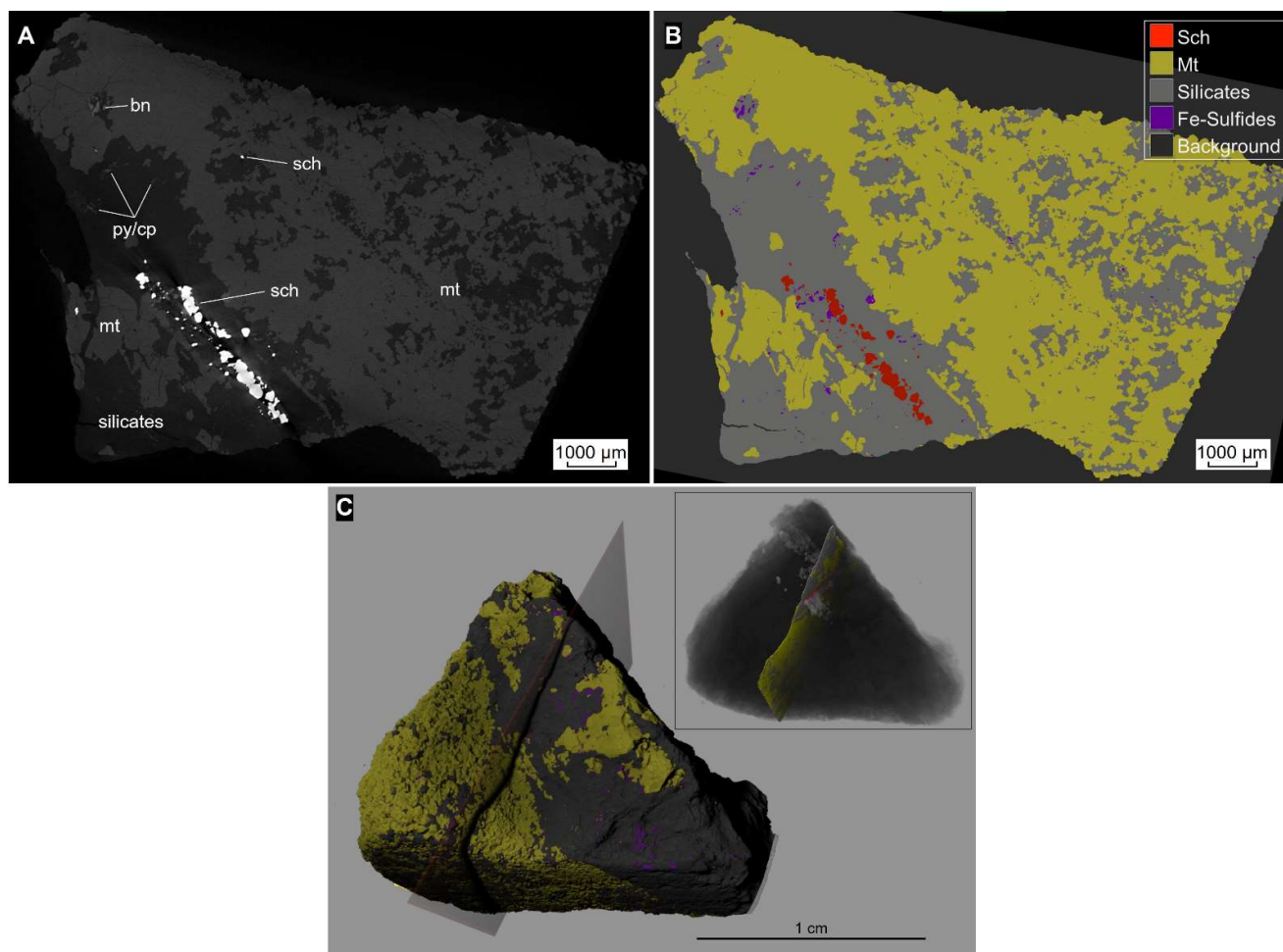


Figure 6. CT volume slice of ROM4 before (A) and after segmentation (B). Volume of the ROM4 sample with the position of the CT volume slice as indicated by the semi-transparent square and the insert image (C). The thickness of the volume slice is 10 μm . Abbreviations: Bn = bornite, cpy = chalcopyrite, mt = magnetite, py = pyrite, sch = scheelite.

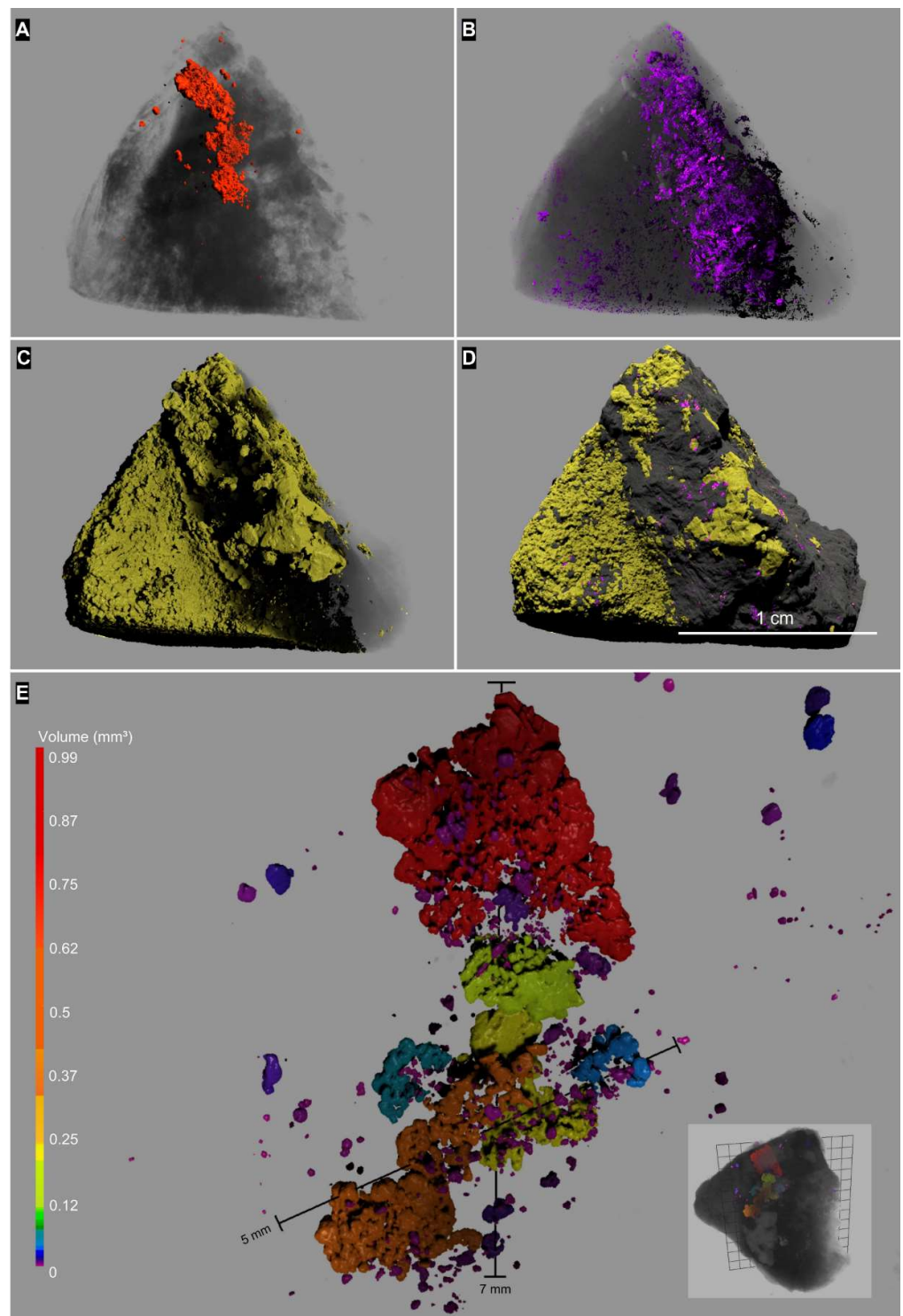


Figure 7. Spatial 3D distribution of the classes defined for the sample ROM4 (A–D). (A) Heterogeneous scheelite mineralisation mainly occurring as vein-fill and a few disseminated particles in the vicinity of the vein. (B) Fe-sulfides are mostly present in the silicate matrix. (C) Magnetite comprising massive aggregates (left) and elongated grains parallel oriented to the dipping direction of the vein. (D) Rendered volume of ROM4 with all segmented classes. Note that scheelite is not visible because it does not occur on the surface in this view. (E) Volumetric distribution of scheelite mineralisation with fractured and subhedral-euhedral grains. The majority of the scheelite volume forms part of the vein. The ore matrix is set to transparent.

5. Discussion

To date, there have been few mineralogical studies of the Kara Fe-W skarn deposit, with one primarily focusing on mineral identification [23], while others explored the development of skarn formation [26,27], in general using predominantly geochemical methods and petrographic data obtained from optical microscopy. This study contributes additional mineralogical insights and introduces CT as a novel approach for investigating ore textures and modal mineralogy in selected samples of the Kara Fe-W deposit with a primary focus on scheelite. Key findings include: (1) scheelite is predominately spatially associated with hydrous silicates; (2) scheelite occurs as massive and fractured or disseminated, with vein-fill mineralisation controlling the majority of the scheelite volume; (3) CT can be successfully applied to study scheelite ore textures in 2D and 3D; (4) CT of scheelite ore allows quantification of its modal mineralogy; and (5) CT analyses permit the quantification of the W grade (WO_3) of ore samples.

5.1. CT Data Acquisition

Previous studies utilising CT for the analysis of scheelite ores relied on conventional segmentation methods. For instance, Le Roux et al. (2015) employed a local thresholding method, successfully differentiating scheelite from gangue and allowing for the quantification of ore grade [20]. Warlo et al. (2021), on the other hand, (qualitatively) determined modal mineralogy using watershed segmentation [21]. While effective for phases with large attenuation differences, these methods yielded unsatisfactory results for phases with similar grey values, exacerbated by acquisition issues such as image noise, beam hardening, and the cupping effect (Figure 3A) [21]. In this study, a deep-learning-based segmentation method was applied, representing the first documented use of application in the context of scheelite ore analysis. Unlike histogram-based segmentation, deep learning algorithms used and trained for segmentation consider additional feature information, such as grain shape and grain boundaries [38]. This consideration minimises the impact of scanning artifacts (Figure 3), sample geometry (ROM4), and overlapping grey values, resulting in a more accurate quantitative analysis, particularly of similar attenuating phases.

The segmentation method employed in this study quantified the entire sample, with the resolution capacity being constrained by the sample size or the system's field of view. The chosen acquisition parameters resulted in voxel sizes of 7.8 μm (ROM1) and 8.4 μm (ROM4) (close to resolution limit of the scanner). Despite this relatively high scanning resolution, certain challenges arise, particularly for the smallest segmented particles which are affected by the partial volume effect (PVE). Considering that a voxel represents the average value of the attenuation coefficients over its volume, the PVE occurs where multiple particles contribute to a single voxel, resulting in blurring intensities of phases and structures. This phenomenon compromises the accuracy of the calculated grain sizes, as well as the representation of real shapes and grain boundaries, and can lead to over- or underestimation of the labelled volume [41]. Even with modern deep learning segmentation models, the PVE cannot be eliminated, as it is inherent to the voxelised data. In the case of ROM1, scheelite is disseminated in the ore and exhibits small grain sizes. At the same time, other dense phases, such as zircon and monazite, are present. As a result, small scheelite grains inevitably suffer from the partial volume effect, showing mixed attenuation coefficients and lower grey values that may overlap with larger zircon and monazite grains. Mixed attenuation coefficients also complicate manual segmentation for establishing training data for the deep learning model, introducing the potential for labelling errors by the operator.

The image noise in the CT data from ROM1 was improved through the fusion of two single CT scans at the same X-ray energy. When aiming to differentiate between as many phases as possible, DECT can also be considered, as it may improve the grayscale contrast between individual phases [35]. This, for example, could potentially reveal if scheelite is preferably attached to a specific hydrous phase as the high-voltage setting applied does decrease image contrast of lower X-ray absorbing phases. Furthermore, to enhance the representation of smaller grains, higher scanning resolution and longer acquisition time should be considered.

Additionally, nano-focused CT sources with resolutions down to hundreds of nanometers can be utilised, but this comes at the cost of scanning smaller sample sizes due to a reduced field of view and thus sample representativity (smaller sample volume). However, in the present study, the proportion of small grains contributing to the total scheelite volume is negligible. The accuracy of the segmentation results was validated by comparing the calculated tungsten grades of the two samples to conventional ICP-OES analysis (Table 5), showing a strong correlation between CT and ICP data. Furthermore, the magnetite content in ROM4 calculated using CT closely matched the results obtained from QXRD measurements (see Figure 5 and Figure A3). This validation underscores the reliability of CT in scheelite ore characterisation.

5.2. Implications of CT Analysis

5.2.1. Scheelite Ore Genesis

The mineral assemblages and the textures observed in the samples studied indicate that they are likely part of stage III skarn formation (as defined by [26]). In addition to scheelite, both samples contain hydrous minerals such as amphibole, epidote, and chlorite, while ROM4 also features massive magnetite, Fe-sulfides (e.g., pyrite, chalcopyrite and bornite). The pervasive texture of hydrous minerals in ROM1 suggests the replacement of earlier phases, indicative of retrograde hydrous skarn conditions. Previous studies further reported that earlier minerals were replaced through pervasive and diffusive replacement, with a minor contribution from filling veins and fissures [26,27]. However, the rendered and segmented volume of ROM1 shows both an ep-chl vein exhibiting a pervasive texture with fuzzy grain boundaries (Figure 4). Similarly, the 3D texture of ROM4 reveals a vein predominately composed of silicates and scheelite (Figure 6). In addition, in both samples, scheelite is distributed within a vein where most of it is aligned parallel to the vein's dipping direction (Figures 4 and 6). This suggests that a larger proportion of mineralisation occurred as vein fills, particularly scheelite mineralisation, than previously reported [26,27]. It is noteworthy that the recognition of coexisting textures was more easily achieved with 3D information than with 2D. Regardless, it is important to consider that the observations were based on two specimens, and further data are needed to confirm this.

Although both samples show similarities (e.g., presence of hydrous minerals and spatial association), they differ significantly in terms of scheelite content. In ROM1, scheelite is present as a trace mineral (550 ppm WO_3). Therefore, although scheelite mineralisation mainly occurred during stage III, it does not necessarily mean mineral assemblages reflecting this stage contain high scheelite concentrations. Given the high amount of magnetite in ROM4, compared to 378 ppm WO_3 , the average WO_3 content of the Kara Fe-W deposit, the results indicate that more scheelite is present when associated with magnetite. This observation aligns with previous observations of Zaw and Singoyi (2000), who state that the majority of scheelite deposition occurred cogenetically with magnetite mineralisation during the late stages of skarn formation [26]. Considering the distribution of scheelite in ROM4, the higher concentration of W could additionally be attributed to a structural controlled vein fill of W-rich fluids. Regardless, additional data are needed to further discuss on the formation model of the Kara Fe-W deposit.

Even though a high scanning resolution was applied, it falls short of offering detailed insights into mineral reactions and grain boundaries, especially notable in the case of ROM1 with fine grained scheelite particles (mixed attenuation coefficients). As a result, a comprehensive examination and discussion of mineral textures, reflecting mineral reactions and intricate replacement processes, is only achievable through additional 2D petrographic methods. On the other hand, however, CT clearly allows the recognition of grain shapes and major mineral textures (e.g., chlorite-epidote). Moreover, the capability for 3D visualisation distinctly highlights the presence of veins containing chlorite, epidote, scheelite, and fluorite, elucidating their spatial association. In fact, the 3D visualisation offers a real benefit to petrographic studies of this type of ore with a preferred textural occurrence (e.g., vein). Additionally, CT can be used to guide subsequent sectioning, when aiming for a higher resolution and obtaining complex petrographic information, e.g., to study the

specific chlorite or epidote texture (ROM1), or to study the mineral chemistry of scheelite that may occur as a trace mineral. Consequently, CT enables a more accurate interpretation of mineralogy, enhancing the understanding of scheelite ore genesis.

5.2.2. Mineral Processing

Pre-concentration of tungsten ores typically involves the use of X-ray sorting, gravitational sorting, optical sorting, or hand-picking methods [42]. At Kara, scheelite is currently extracted as a by-product of magnetite, with scheelite being screened using handheld UV light devices. These conventional (mainly 2D) processing techniques rely on exposing scheelite to the ore surfaces for proper pre-concentration, potentially overlooking scheelite grains buried within the rock mass hindering complete recovery. In the CT data, scheelite exhibits the highest X-ray attenuation compared to other minerals in the ore. The application of CT for qualitative analysis to determine scheelite occurrence enables rapid data acquisition without the need for subsequent segmentation. In particular, CT could be employed for scheelite screening during comminution for process control and monitoring. Consequently, CT may contribute to a more efficient screening of ore and waste material at the Kara Fe-W mine.

Understanding the spatial distribution of ore and gangue minerals is also useful to achieve more efficient mineral processing of the mined ores. By obtaining information on particle size distribution, morphology, and occurrence before and after comminution using CT, the yield of the process could be quantified based on these properties analysed in situ. As scheelite is a brittle mineral, and particles smaller 20 μm (very fines as defined by [43]) are difficult to recover [44], the spatial arrangement of scheelite should be considered in the choice of the comminution steps to preserve grain size and thus maximise recovery. Understanding the natural grain size of scheelite is crucial for anticipating potential losses during processing. For instance, if scheelite naturally occurs in sizes all under 20 μm , recovery becomes exceedingly difficult. Grain size information obtained with CT allows for the estimation of the proportion of scheelite of natural size likely to be lost to very fines. If scheelite is predominantly large in size, its size reduction during comminution (crushing and grinding steps) can be optimised to minimise losses in the processing circuit. This comprehensive understanding of recovery potential aids in optimising mineral recovery and achieving resource efficiency.

6. Conclusions

This study has provided novel mineralogical insights of the Kara Fe-W ore, Tasmania, Australia. The results indicate that scheelite is predominately spatially associated with hydrous silicates and occurs massive or disseminated with vein-fill mineralisation controlling a significant portion of its volume. CT proves effective in analysing the texture of scheelite ore in both 2D and 3D, further allowing for the examination of major, minor, and trace mineral phases with given grey value contrasts and particle sizes. CT falls short of offering detailed insights into mineral reactions and grain boundaries, especially of fine-grained particles and the quantification of similar X-ray attenuating phases (e.g., chlorite and epidote). A comparison with ICP-OES and XRD showed that CT is reliable for quantifying modal mineralogy and assessing WO_3 grade in individual ore samples. Integrating CT with conventional 2D techniques holds promise for enhancing our understanding of the formation and mineralisation processes of Fe-W deposits. Furthermore, the insights provided by CT may inform the optimisation of scheelite extraction and separation techniques, thereby fostering more efficient resource recovery practices at the Kara mine.

Author Contributions: Conceptualisation, L.T.K. and J.A.H.; methodology, L.T.K.; software, L.T.K.; formal analysis, L.T.K.; investigation, L.T.K.; data curation, L.T.K.; writing—original draft preparation, L.T.K.; writing—review and editing, L.T.K., B.G.L. and J.A.H.; visualisation, L.T.K.; supervision, B.G.L. and J.A.H.; project administration, L.T.K.; funding acquisition, B.G.L. and J.A.H. All authors have read and agreed to the published version of the manuscript.

Funding: This research received no external funding.

Data Availability Statement: Data supporting the findings of this study will be made available from the corresponding author, upon reasonable request.

Acknowledgments: Access to and sampling at the Kara mine was allowed by the Kara mine site staff, which is gratefully acknowledged. Two anonymous reviewers are thanked for their constructive feedback that improved the manuscript.

Conflicts of Interest: The authors declare no conflict of interest.

Appendix A

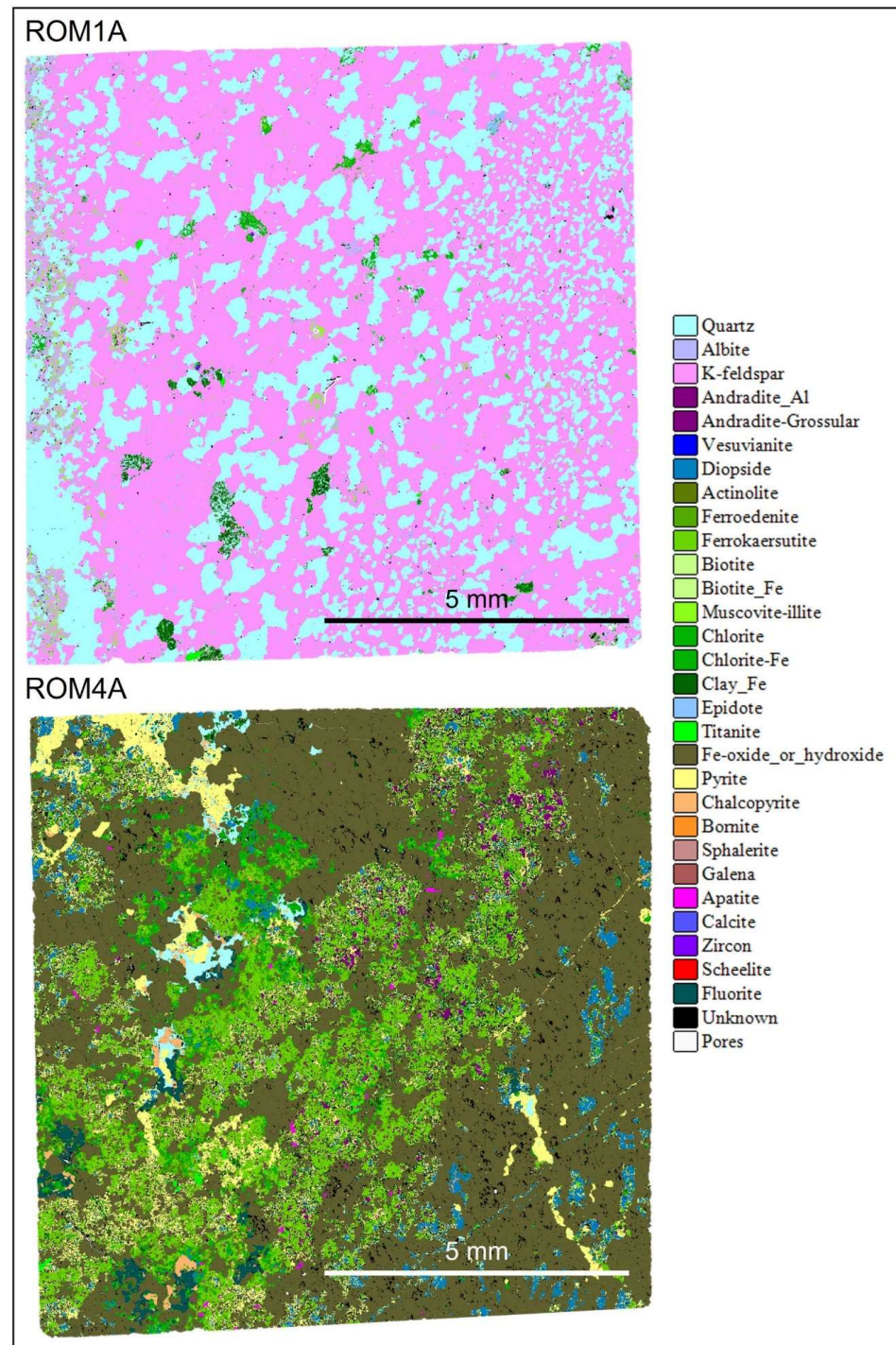


Figure A1. AMICS data of the two ore samples (ROM1 and ROM4) studied.

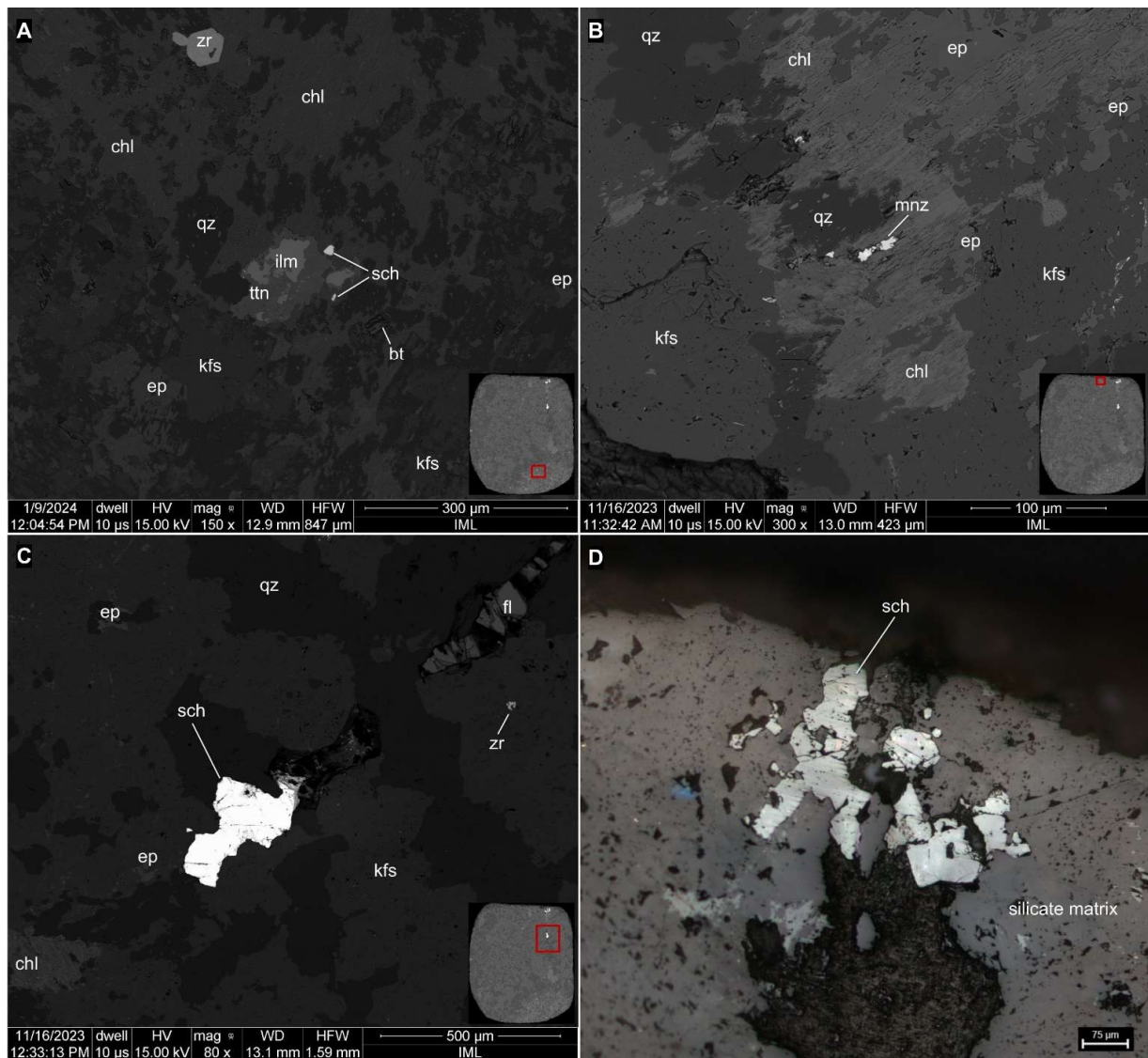


Figure A2. SEM images (A–C) and a microphotograph (D) of the ROM1 sample.

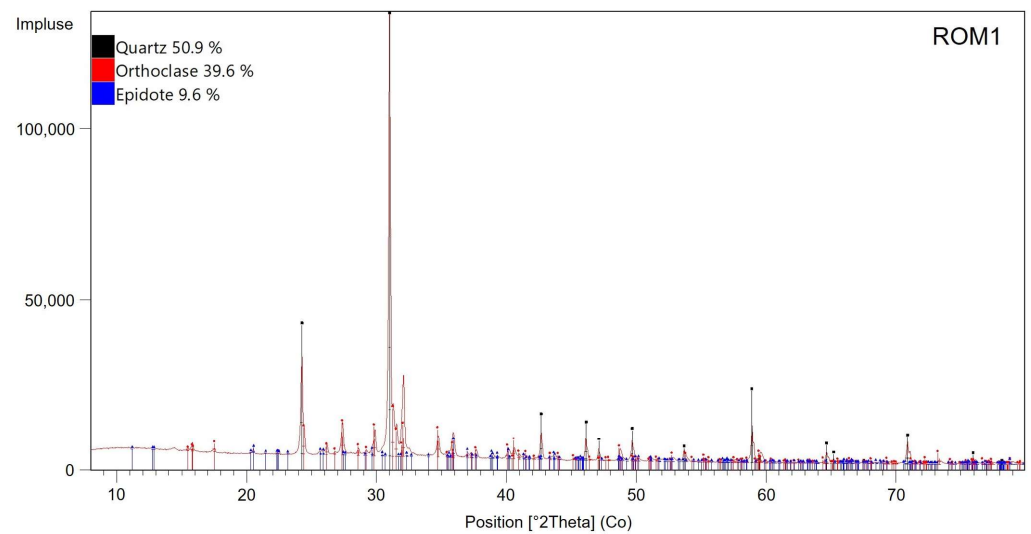


Figure A3. Cont.

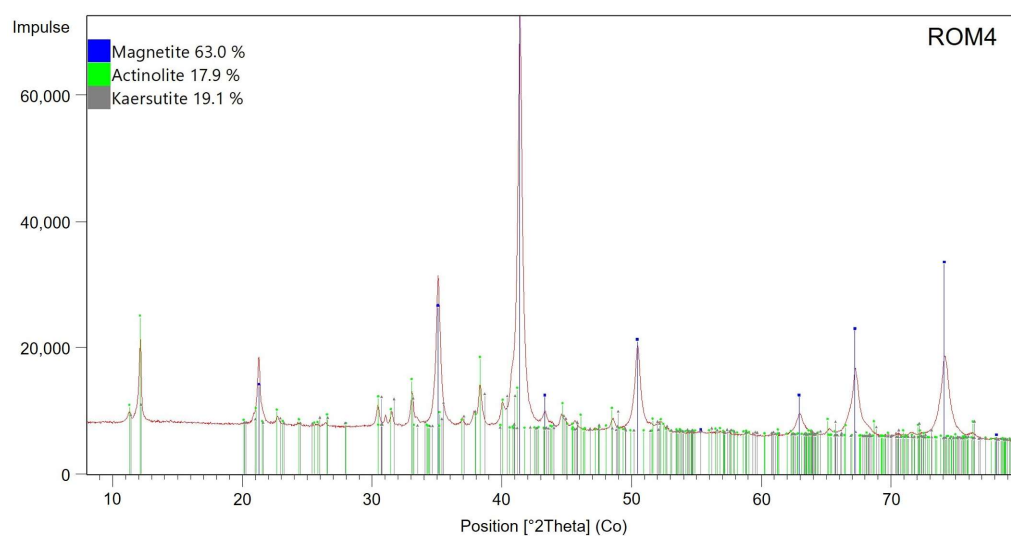


Figure A3. XRD patterns of the samples investigated. The undefined peak at 14.4 2θ in the XRD pattern of ROM1 is chlorite. However, it was not identified by the Highscore software.

References

- Pitfield, P.; Brown, T.; Rayner, D. *Tungsten Profile*; British Geological Survey: Nottingham, UK, 2011.
- European Commission. *Study on the EU's List of Critical Raw Materials*; European Commission: Brussels, Belgium, 2020.
- Sandler, R.B. *Tungsten*; U.S. Geological Survey: Reston, VA, USA, 2023.
- Hughes, A. *Australian Resource Reviews Tungsten*; Geoscience Australia, Canberra: Symonston, Australia, 2020.
- Todesco, R. The Tungsten Revival. *Mining Magazine*. 2023. Available online: <https://miningmagazine.com.au/the-tungsten-revival/> (accessed on 1 March 2024).
- Butcher, A.R.; Dehaine, Q.; Menzies, A.H.; Michaux, S.P. Characterisation of Ore Properties for Geometallurgy. *Elements* **2023**, *19*, 352–358. [[CrossRef](#)]
- Zhan, Q.; Gao, X.-Y.; Meng, L.; Zhao, T.-P. Ore genesis and fluid evolution of the Sandaozhuang supergiant W-Mo skarn deposit, southern margin of the North China Craton: Insights from scheelite, garnet and clinopyroxene geochemistry. *Ore Geol. Rev.* **2021**, *139*, 104551. [[CrossRef](#)]
- Miranda, A.C.R.; Beaudoin, G.; Rottier, B. Scheelite chemistry from skarn systems: Implications for ore-forming processes and mineral exploration. *Min. Depos.* **2022**, *57*, 1469–1497. [[CrossRef](#)]
- Soloviev, S.G. Geology, mineralization, and fluid inclusion characteristics of the Kumbel oxidized W-Cu-Mo skarn and Au-W stockwork deposit in Kyrgyzstan, Tien Shan. *Min. Depos.* **2015**, *50*, 187–220. [[CrossRef](#)]
- Withers, P.J.; Bouman, C.; Carmignato, S.; Cnudde, V.; Grimaldi, D.; Hagen, C.K.; Maire, E.; Manley, M.; Du Plessis, A.; Stock, S.R. X-ray Computed Tomography. *Nat. Rev. Methods Primers* **2021**, *1*, 18. [[CrossRef](#)]
- Krebbbers, L.; Gainov, R.; Lottermoser, B.G.; Lohmeier, S.; Hennig, A. Applications of Industrial Computed Tomography in the Mining Sector. *Min. Rep. Glückauf* **2020**, *157*, 360–369.
- Mees, F.; Swennen, R.; van Geet, M.; Jacobs, P. *Applications of X-ray Computed Tomography in the Geosciences*; Geological Society Publishing House: Bath, UK, 2003; ISBN 9781862391390.
- Cnudde, V.; Boone, M.N. High-resolution X-ray computed tomography in geosciences: A review of the current technology and applications. *Earth-Sci. Rev.* **2013**, *123*, 1–17. [[CrossRef](#)]
- Guntoro, P.I. X-ray Microcomputed Tomography (μ CT) as a Potential Tool in Geometallurgy. Ph.D. Thesis, Luleå University of Technology, Luleå, Sweden, 2019.
- Krebbbers, L.T.; Lottermoser, B.G.; Liu, X. Computed tomography of flake graphite ore: Data acquisition and image processing. *Minerals* **2023**, *13*, 247. [[CrossRef](#)]
- Kyle, J.R.; Ketcham, R.A. Application of high resolution X-ray computed tomography to mineral deposit origin, evaluation, and processing. *Ore Geol. Rev.* **2015**, *65*, 821–839. [[CrossRef](#)]
- Ferraz da Costa, M.; Kyle, J.R.; Lobato, L.M.; Ketcham, R.A.; Figueiredo e Silva, R.C.; Fernandes, R.C. Orogenic gold ores in three-dimensions: A case study of distinct mineralization styles at the world-class Cuiabá deposit, Brazil, using high-resolution X-ray computed tomography on gold particles. *Ore Geol. Rev.* **2022**, *140*, 104584. [[CrossRef](#)]
- Chisambi, J.; von der Heyden, B.P.; Tshibalanganda, M.; Le Roux, S.G. Gold Exploration in Two and Three Dimensions: Improved and Correlative Insights from Microscopy and X-Ray Computed Tomography. *Minerals* **2020**, *10*, 476. [[CrossRef](#)]
- Lohmeier, S.; Gainov, R.R.; Hodgkin, A. Morphological characterization of lode gold in the auriferous quartz veins at M'Popo mine, Angola, by computed tomography and optical microscopy. *Appl. Earth Sci.* **2023**, *132*, 65–89. [[CrossRef](#)]

20. Le Roux, S.G.; Du Plessis, A.; Rozendaal, A. The quantitative analysis of tungsten ore using X-ray microCT: Case study. *Comput. Geosci.* **2015**, *85*, 75–80. [[CrossRef](#)]
21. Warlo, M.; Bark, G.; Wanhainen, C.; Butcher, A.R.; Forsberg, F.; Lycksam, H.; Kuva, J. Multi-Scale X-ray Computed Tomography Analysis to Aid Automated Mineralogy in Ore Geology Research. *Front. Earth Sci.* **2021**, *9*, 789372. [[CrossRef](#)]
22. Rozendaal, A.; Le Roux, S.G.; Du Plessis, A. Application of microCT scanning in the recovery of endo-skarn associated scheelite from the Riviera Deposit, South Africa. *Miner. Eng.* **2017**, *116*, 163–178. [[CrossRef](#)]
23. Barret, D.E. *Geology, Mineralogy and Conditions of Formation of the Kara Scheelite Skarn*; University of Tasmania: Hobart, Australia, 1980.
24. Fudge, A.D. Kara No. 1 Magnetite Deposit Ore Reserve Report January 2016. Available online: https://minedocs.com/17/TasmaniaMines_Ore_Reserve_2016.pdf (accessed on 21 March 2024).
25. Callaghan, T. Kara No. 1 Mineral Resource Estimate. Available online: <https://www.asx.com.au/asxpdf/20150218/pdf/42wpdfqky18shb.pdf> (accessed on 21 March 2024).
26. Zaw, K.; Singoyi, B. Formation of Magnetite-Scheelite Skarn Mineralization at Kara, Northwestern Tasmania: Evidence from Mineral Chemistry and Stable Isotopes. *Econ. Geol.* **2000**, *95*, 1215–1230. [[CrossRef](#)]
27. Singoyi, B.; Zaw, K. A petrological and fluid inclusion study of magnetite-scheelite skarn mineralization at Kara, Northwestern Tasmania: Implications for ore genesis. *Chem. Geol.* **2001**, *173*, 239–253. [[CrossRef](#)]
28. Collins, P.L.F.; Brown, S.G.; Dronseika, E.V.; Morland, R. *Mid-Paleozoic Ore Deposits*; Geological Society of Australia Special Publication: Parkes, Australia, 1989; pp. 270–292.
29. Banks, M.R.; Baillie, P.W. Late Cambrian to Devonian. *Geol. Miner. Resour. Tasman.* **1989**, *15*, 182–237.
30. Leaman, D.E.; Richardson, R.G. Production of a Residual Gravity Field Map for Tasmania and Some Implications. *Explor. Geophys.* **1989**, *20*, 181–184. [[CrossRef](#)]
31. Williams, E.; McClenaghan, M.P.; Collins, P.L.D. *Mid-Paleozoic Deformation, Granitoid and Ore Deposits*; Geological Society of Australia Special Publication: Parkes, Australia, 1989; Volume 15, pp. 238–292.
32. Berry, R.F. The history of movement on the Henty Fault Zone, western Tasmania: An analysis of fault striations. *Aust. J. Earth Sci.* **1989**, *36*, 189–205. [[CrossRef](#)]
33. Stock, S.R. *MicroComputed Tomography: Methodology and Applications*, 2nd ed.; CRC Press: Boca Raton, FL, USA, 2019; ISBN 9780429186745.
34. van Grieken, R.; Markowicz, A. *Handbook of X-Ray Spectrometry*; CRC Press: Boca Raton, FL, USA, 2001; ISBN 9780203908709.
35. Krebbers, L.T.; Grozmani, N.; Lottermoser, B.G.; Schmitt, R.H. Dual-energy computed tomography for improved contrast on a polyphase graphitic ore. *Tomogr. Mater. Struct.* **2024**, *4*, 100021. [[CrossRef](#)]
36. Volume Graphics GmbH. *VGSTUDIO MAX 3.5.1*; Volume Graphics: Heidelberg, Germany, 2021.
37. Object Research Systems. *Dragonfly*; Object Research Systems: Montreal, QC, Canada, 2022.
38. Novikov, A.; Major, D.; Wimmer, M.; Lenis, D.; Bühler, K. Deep Sequential Segmentation of Organs in Volumetric Medical Scans. *IEEE Trans. Med. Imaging* **2019**, *38*, 1207–1215. [[CrossRef](#)]
39. Berger, M.J.; Hubbell, J.H.; Seltzer, S.M.; Chang, J.; Coursey, J.S.; Sukumar, R.; Zucker, D.S.; Olsen, K. X-COM: Photon Cross Sections Database. Available online: <https://www.nist.gov/pml/xcom-photon-cross-sections-database> (accessed on 5 December 2023).
40. Li, X.; Zhang, G.; Li, K.; Zheng, W. Deep Learning and Its Parallelization. In *Big Data: Principles and Paradigms*; Buyya, R., Calheiros, R.N., Dastjerdi, A.(E.)V., Eds.; Elsevier/Morgan Kaufmann: Cambridge, MA, USA, 2016; pp. 95–118. ISBN 978-0-12-805394-2.
41. Kyle, J.R.; Mote, A.S.; Ketcham, R.A. High resolution X-ray computed tomography studies of Grasberg porphyry Cu-Au ores, Papua, Indonesia. *Min. Depos.* **2008**, *43*, 519–532. [[CrossRef](#)]
42. Yang, X. Beneficiation studies of tungsten ores—A review. *Miner. Eng.* **2018**, *125*, 111–119. [[CrossRef](#)]
43. Sivamohan, R.; Forssberg, E. Recovery of heavy minerals from slimes. *Int. J. Miner. Process.* **1985**, *15*, 297–314. [[CrossRef](#)]
44. Krishna Rao, N. Beneficiation of tungsten ores in India: A review. *Bull. Mater. Sci.* **1996**, *19*, 201–265. [[CrossRef](#)]

Disclaimer/Publisher’s Note: The statements, opinions and data contained in all publications are solely those of the individual author(s) and contributor(s) and not of MDPI and/or the editor(s). MDPI and/or the editor(s) disclaim responsibility for any injury to people or property resulting from any ideas, methods, instructions or products referred to in the content.